buildings

MDPI

Article

Investigation of the Hysteresis Performance of Multi-Story Y-Shaped Eccentrically Bare Braced Steel Frame with Block Slit Damper (BSD)

Chen Zhou [1], Haibo Wen [1,*], Jing Zhao [2], Lizhong Jiang [1], Xiaodong Xu [3], Hong Zheng [3], Yuxiao Tian [4], Muhua Liang [4], Xiyao Wang [2] and Hai Zhang [4]

[1] School of Civil Engineering, Central South University, Changsha 410075, China; 13578623580@126.com (C.Z.); lzhjiang@csu.edu.cn (L.J.)
[2] 3rd Construction Co., Ltd., China Construction 5th Engineering Bureau, Changsha 410004, China; yiyun21709@163.com (J.Z.); cscec53hnhw@163.com (X.W.)
[3] School of Civil Engineering, Chang'an University, Xi'an 710061, China; 21020201085@mail.hnust.edu.cn (X.X.); cehzheng@chd.edu.cn (H.Z.)
[4] China Railway Urban Construction Group Co., Ltd., Changsha 410036, China; zjq54610@163.com (Y.T.); 13786282768@139.com (M.L.); fusu0116@126.com (H.Z.)
* Correspondence: haibowen_2000@163.com

Abstract: This paper investigated the hysteresis performance of multi-story Y-shaped eccentrically bare braced steel frames with block slit dampers (BSDs). After validating existing models through finite element (FE) analysis, an FE model of Y-shaped eccentrically bare braced steel frames (YEBFs) with BSD (BSD-YEBFs) was established. The influences of different types of BSDs on the hysteresis performance of YEBFs were subsequently analysed, as were the seismic performances of YEBFs with BSD (BSDF) and traditional Y-shaped eccentrically bare braced steel frames (TEBF) under cyclic loading, including the stress failure mode, hysteresis curve, stiffness, strength, and energy dissipation capacity. The results showed that: (1) compared with those of BASE-Y, the ductility coefficients of YEBFs with one level BSD (BSD-1) and two level BSD (BSD-2) increased by 59.57% and 39.47%, respectively, and the lateral bearing capacity decreased by 3.26% and 2.78%, respectively. (2) Compared with those of TEBF, the yield bearing capacity and ultimate bearing capacity of BSDF increased by 3.13% and 11.12%, respectively, and the ductility coefficient increased by 56.7%. Moreover, BSDF possesses higher initial stiffness and more sustained energy dissipation capabilities.

Keywords: Y-shaped eccentrically bare braced steel frames; block slit dampers (BSDs); hysteresis performance; finite element modeling

Academic Editor: Duc-Kien Thai

Received: 7 December 2024
Revised: 20 December 2024
Accepted: 26 December 2024
Published: 31 January 2025

Citation: Zhou, C.; Wen, H.; Zhao, J.; Jiang, L.; Xu, X.; Zheng, H.; Tian, Y.; Liang, M.; Wang, X.; Zhang, H. Investigation of the Hysteresis Performance of Multi-Story Y-Shaped Eccentrically Bare Braced Steel Frame with Block Slit Damper (BSD). *Buildings* **2025**, *15*, 451. https://doi.org/10.3390/buildings15030451

1. Introduction

Earthquakes are highly hazardous natural disasters characterized by uncertainty and contingency. Each outbreak poses a threat to human life and property safety. Steel structures have been widely used in buildings because of their excellent seismic performance [1,2].

In many earthquake-resistant areas of China, multi-story steel structure buildings usually adopt a bending steel frame structure composed of frame beams and frame columns with good energy dissipation and ductility performance. However, the lateral stiffness of steel frames is relatively low, and setting eccentric braces in the steel frame can effectively improve this situation. Eccentrically braced steel frame (EBF) structures represent effective seismic-resistant systems. During seismic events, these structures utilize the

plastic deformation of energy-dissipating beam sections to dissipate seismic energy, limiting brace buckling and maintaining overall structural stability [3,4]. Currently, many works have tested different types of EBFs, and the results show that EBFs can significantly improve the seismic resistance of steel frame structures [5–10]. Eccentric braces can be categorized into various types, such as D-type, K-type, V-type and Y-type braces, on the basis of their geometric configuration. Compared with other braces, the Y-shaped eccentric braces (Figure 1a) have relatively high independence because the energy-dissipating beam section is set separately below the frame beam. Xiao et al. [6] conducted a study on the seismic performance of Y-type EBF and K-type EBF under seismic action, and the results indicated that the Y-type EBF has superior energy dissipation capabilities compared with the K-type EBF. Wang et al. [10] evaluated the seismic performance of four types (D, K, Y, and V) of EBF structures via pushover analysis and nonlinear time-history dynamic analysis, and the findings demonstrated that the Y-shaped EBF exhibited better ductility.

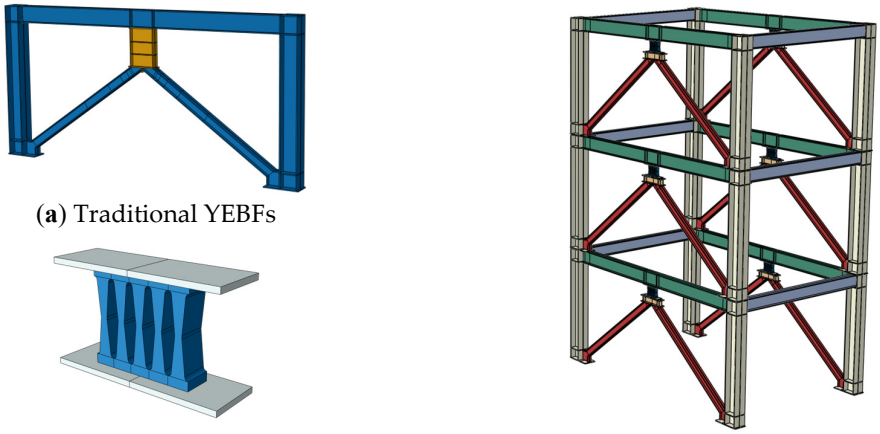

(**a**) Traditional YEBFs

(**b**) Block slit damper

(**c**) YEBFs with BSD

Figure 1. Schematic diagram of steel frames and dampers.

However, under strong seismic events, the energy-dissipating beam section of EBF structures may reach their ultimate deformation, potentially leading to severe structural damage. Concurrently, significant residual deformation of a structure can result in a complex and costly post-earthquake repair process [11,12]. It is necessary to further enhance the ductility and energy dissipation capacity of the energy-dissipating beam section in EBF structures to reduce the damage and residual deformation in these sections, thus adapting to the higher seismic fortification standards currently proposed. Many studies have considered the use of dampers, including viscous dampers [13], friction dampers [14], and metal dampers [15], to enhance the seismic performance of steel frames. Zhao et al. [16] utilized a novel bent shear panel damper to improve the seismic performance of YEBFs, thereby reducing damage to concrete slabs under seismic loading. Li et al. [17] explored the application of a demountable-metallic-corrugated-shear-panel damper (DCSPD) in YEBFs and evaluated the dynamic seismic performance of DCSPDs through dynamic time history analysis and seismic fragility analysis. Mirzai et al. [18] investigated the application of self-centring dampers in YEBFs, which consist of a combination of shape memory alloy (SMA) and lead rubber damper (LRD). This device utilizes the self-centring characteristics of SMA and the energy dissipation capabilities of LRD to enhance the seismic performance of structures. Meanwhile, several studies [1,19] have considered employing easily replaceable energy dissipation devices within the EBF structures. In addition, there has been considerable interest in the application of negative Poisson's ratio (NPR) materials in dampers [20]; NPR structures are capable of significantly enhancing

energy dissipation by undergoing substantial plastic deformations under both tensile and compressive stresses.

As is well known, metal dampers dissipate energy through the plastic deformation of their constitutive materials, offering advantages such as simple construction, stable hysteresis performance, and low-temperature sensitivity [21,22]. Recently, Amiri et al. [21] introduced a novel type of metal damper known as the block slit damper (BSD), which consists of a steel block with several slits and two steel plates (Figure 1b). This assembly provides high bearing capacity while maintaining the ability to dissipate energy continuously under large displacements. Their findings also revealed that as the aspect ratio (h_0/b_1) decreased, the shear and energy dissipation capabilities were augmented, whereas the displacement capacity was diminished. Subsequent research [23] utilized the endurance time (ET) dynamic analysis method to evaluate the horizontal seismic performance of low-rise steel frame structures equipped with BSDs. Mohseni et al. [24] employed numerical simulation methods to investigate the impact of BSD geometric parameters on seismic energy absorption.

Given the aforementioned information, this study proposed a YEBF with a block slit damper, as shown in Figure 1c. The hysteresis performance of YEBFs with different types of BSDs was investigated via the FE software ABAQUS 6.14. Furthermore, a detailed comparative analysis was conducted between YEBF with BSD (BSDF) and traditional YEBF (TEBF) to evaluate their hysteresis performance under cyclic loading. This work aimed to provide insights into the use of BSDs in YEBF structures.

2. FE Model Validation

2.1. Establishment of the FE Model

To validate the accuracy of the EBF model, this study established an FE model of specimen Y-1 from the 1/3 scale single-span, two-story frame test in reference [25] according to the relevant provisions of the Chinese standard (GB 50011-2010; JGJ 99-2015; GB 50017-2017) [26–28]. A schematic diagram of the YEBF is shown in Figure 2, and the detailed dimensions of the relevant components are presented in Table 1.

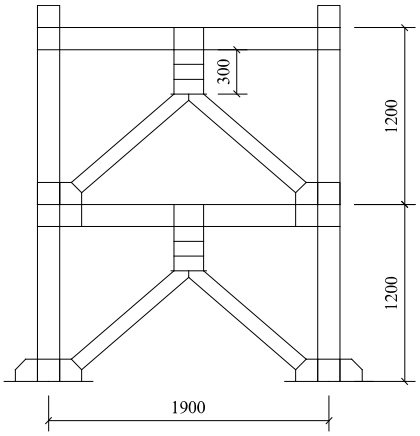

Figure 2. Dimensions of YEBF in reference [22] (unit: mm).

Table 1. Section size of each component of specimen Y-1 (unit: mm).

Element	Section ($h \times b_f \times t_w \times t_f$)
Column	H150 × 150 × 7 × 10
Beam	H150 × 150 × 7 × 10
Brace	H100 × 100 × 7 × 10
Energy Dissipation Beam	H200 × 100 × 5.5 × 8

In the experiment, all of the components were made of Q235 steel, with an elastic modulus of 206,000 MPa and a Poisson's ratio of 0.3. Detailed information regarding the material properties is shown in Table 2.

Table 2. Properties of the steel material.

Steel	σ_y/MPa	ε_y	σ_u/MPa	ε_u	σ_{st}/MPa	ε_{st}
Q235	235	0.001	420	0.15	330	0.22
Q355	355	0.002	550	0.116	450	0.17

The following assumptions are made regarding the properties of steel materials: (1) the steel material is homogeneous and isotropic; (2) initial defects in the steel are not considered; and (3) the yield criterion adopts the von Mises criterion. To accurately simulate the stress situation of steel under low-cycle reversed loading and large deformations [29] while taking into account the influence of the Bauschinger effect on steel properties, a multilinear mixed strengthening criterion and a tri-linear model with a descending segment were adopted, as shown in Figure 3.

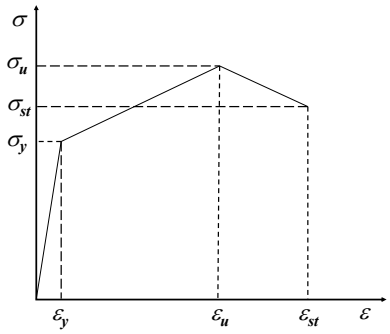

Figure 3. Stress–strain relationship of steel.

A three-dimensional solid hexahedral nonconforming element model (C3D8I) was employed to establish the YEBF model. The sharp parts of the bracing members were transitioned using a limited number of six-node mother prismatic elements (C3D6). The boundary conditions of the FE model are defined as follows: the frame columns and gusset plates are rigidly connected to the ground (U1 = U2 = U3 = UR1 = UR2 = UR3 = 0); and lateral constraints in the X direction of the frame beams (U1 = 0) are applied to restrict out-of-plane instability of the sample, as shown in Figure 4.

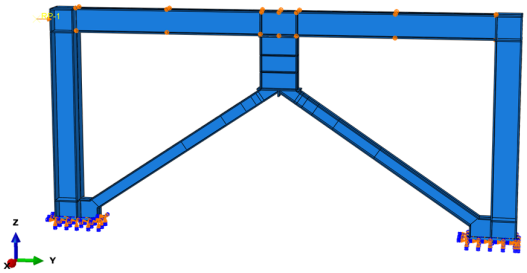

Figure 4. Boundary conditions.

The FE loading protocol adheres to the complete loading system specified in the standard [30]: 0.25 Δ_y, 0.5 Δ_y, 0.75 Δ_y, 1 Δ_y, 2 Δ_y, 3 Δ_y, 4 Δ_y, 5 Δ_y. . ., where Δ_y represents the yield displacement of the sample. Each loading increment is cycled twice, as shown in Figure 5.

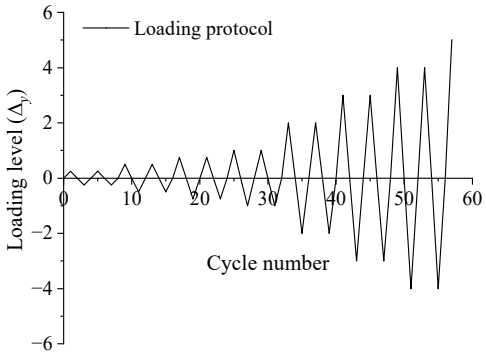

Figure 5. Loading protocol.

According to the calculation results, the grid size was adjusted as follows: the element size for the frame beams and frame columns was set to 60 mm, whereas the element size for the eccentric bracing members was 30 mm. To analyse the stress–strain conditions of the energy-dissipating beam section precisely, the grid in these areas was refined, with each plate component having an element size of 20 mm, as shown in Figure 6.

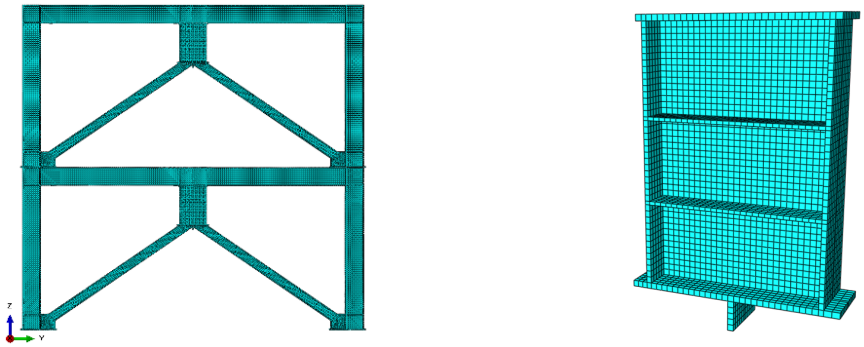

(**a**) Grid division of the steel frame. (**b**) Energy dissipation beam

Figure 6. Grid division of specimen Y-1.

2.2. Comparison of the FEM and Test Results

Figure 7 shows the failure modes of specimen Y-1 from both the experimental and FE analysis results. It is evident that the specimen experienced tearing and failure of the weld seam at the connection between the web plate and end plate of the energy dissipation beam section, as well as at the connection between the energy dissipation beam section and the flanges. The FE simulation results show that the failure locations are consistent with the experimental results and indicate that the stress values at these locations are significantly higher than the ultimate stress of the steel.

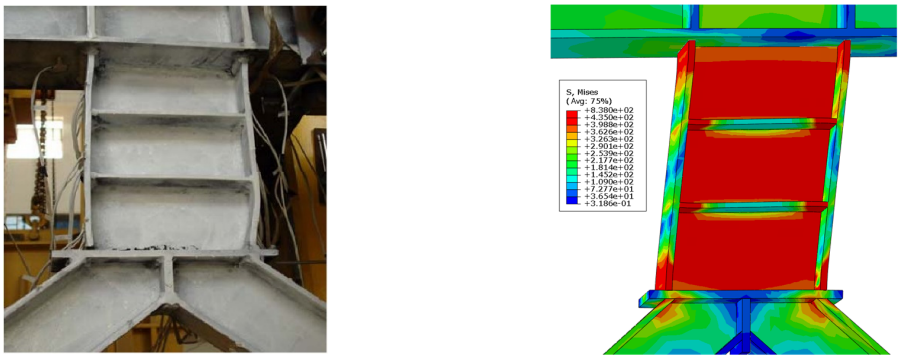

(**a**) Failure mode of Test (**b**) Failure mode of FE simulation

Figure 7. Failure mode of specimen Y-1.

The hysteresis and skeleton curves of specimen Y-1 from both the FE analysis and experimental tests are presented in Figure 8. The hysteresis curves of the two results are symmetrical and full, with a shape similar to a shuttle, and the enveloping areas of the hysteresis loops at each loading stage are roughly equal. The detailed parameters are shown in Table 3. Compared with the experimental results, the buckling load in the FE analysis results decreased by 4.89% (increased by 0.53% in the negative direction), and the ultimate load decreased by 3.96% (increased by 2.35% in the negative direction). The reasons for this error may include the following two points: (1) The FE simulation is more idealized than the experimental simulation is, without considering defects such as steel properties and weld stress, and the constraint conditions for complete rigidity at the bottom of the column cannot be guaranteed during the experiment, resulting in slightly greater initial stiffness in the FE simulation than in the experiment; (2) the material constitutive relationship in the finite element simulation is a tri-linear model, but during the experimental loading, as the steel enters the plastic development stage, its stress–strain relationship is not linear.

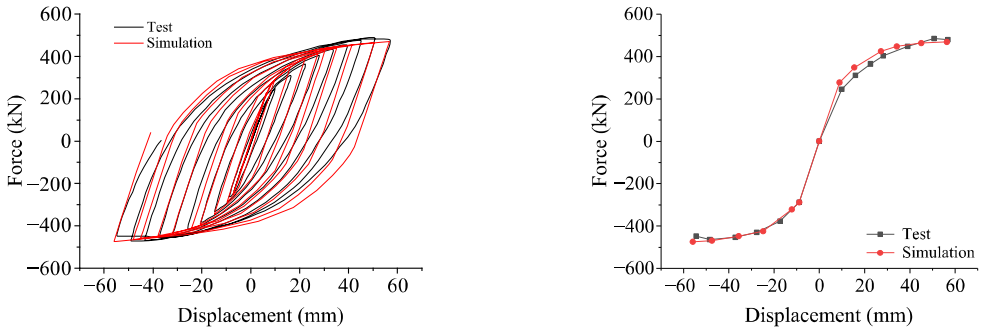

(**a**) Hysteresis curves (**b**) Backbone curves

Figure 8. Comparison of hysteresis curves and backbone curves of specimen Y-1.

Table 3. Comparison of the analytical and experimental results.

Parameter	Loading Direction	Test	FEM	Error
P_y/kN	Positive	401.27	381.66	4.89%
	Negative	−386.24	−388.26	0.53%
P_{max}/kN	Positive	488.45	469.09	3.96%
	Negative	−463.64	−474.54	2.35%

In summary, the force-displacement curves obtained from the FE simulation and experiments exhibit similar shapes, with a high degree of agreement. In terms of the mechanical performance indicators, the errors between the two are within a reasonable range. The FE modelling method used in this paper can accurately simulate the stress characteristics of the YEBFs and provide braces for subsequent research.

3. Influence of BSD on the Hysteresis Performance of YEBFs

3.1. BSD-YEBFs Model

Based on the geometric dimensions of the specimen BASE-Y in reference [31], this section established a traditional YEBFs model and a YEBFs model equipped with BSD-1 and BSD-2. The thickness of the stiffeners is 20 mm, and the cross-sectional dimensions of the frame are presented in Table 4. A schematic diagram of the BSD-YEBF is shown in Figures 9 and 10, with the detailed dimensions of BSD-1 and BSD-2 provided in Table 5.

Table 4. Section size of each component of YEBF (unit: mm).

Element	Section ($h \times b_f \times t_w \times t_f$)
Column	H400 × 400 × 16 × 20
Beam	H400 × 400 × 16 × 20
Brace	H200 × 200 × 12 × 16
Joist	H200 × 100 × 12 × 16

Table 5. Dimensions of BSD-1 and BSD-2 (unit: mm).

Specimen	H	h_0/b_1	b_1	b_2	t	h_u	h_d	r_1	r_2
BSD-1	330	240	45	30	60	30	30	35	15
BSD-2	200	150	30	15	60	30	15	20	10

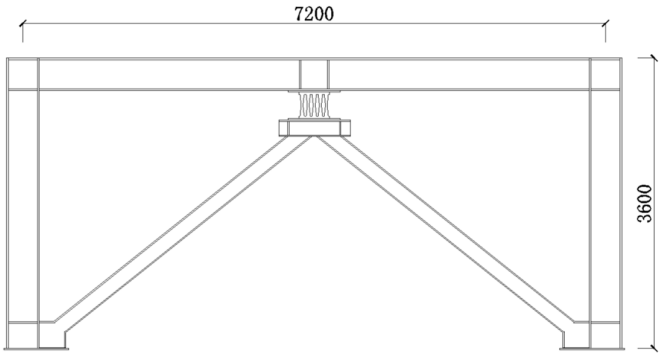

Figure 9. Schematic diagram of BSD-YEBF (unit: mm).

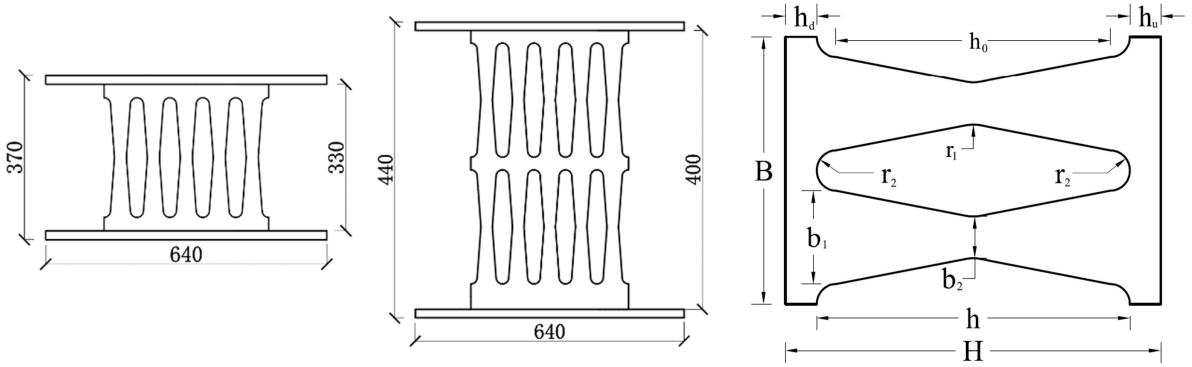

(**a**) BSD-1 (**b**) BSD-2 (**c**) Steel strip

Figure 10. Schematic diagram of BSD-1 and BSD-2 (unit: mm).

In this model, the frame beams, frame columns, and stiffeners of the joist are fabricated from Q355 steel, whereas all other components are made from Q235 steel. The steel has an elastic modulus of 206,000 MPa and a Poisson's ratio of 0.3; additional properties are presented in Table 2.

In addition, the columns and beams, BSD devices and their connected frame beams, as well as the joists, are all constrained via "Tie" constraints to bind them together; The bracing members and bracing feet, columns and their stiffeners, beams and their stiffeners, and joists and their stiffeners are merged into a whole via "Merge". The boundary conditions and loading method are consistent with those in the previous section; notably, each loading level cycle is set to three times.

Figure 11 shows the grid division of the BSD-YEBF. The energy dissipation steel strips of the BSD are divided into C3D6 elements. To analyse the stress–strain variation of the

BSD device's energy dissipation steel strips accurately, the grid in this region is refined with an element size of 10 mm. The grid division and element sizes for the remaining components are consistent with those described in the previous section.

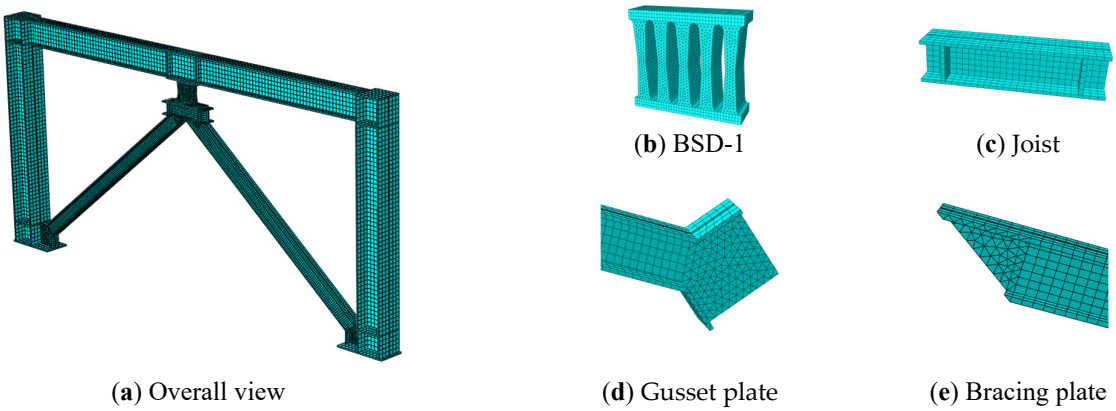

(**a**) Overall view (**b**) BSD-1 (**c**) Joist (**d**) Gusset plate (**e**) Bracing plate

Figure 11. Grid division of BSD-YEBF structure.

3.2. Results Analysis and Comparison

Figure 12 shows the force-displacement curves of samples BASE-Y, BSD-1, and BSD-2. Their hysteresis curves are symmetrical and full, with a shape similar to a shuttle. Specimen BASE-Y experienced premature failure due to buckling of the web in the energy-dissipating beam section, resulting in a continuous decrease in the area enclosed by its hysteresis curve; in contrast, the area enclosed by the hysteresis curve of specimen BSD-1 increased with increasing loading displacement. When loaded to 6 Δ_y, the compressed bracing member experienced bending buckling, which triggered the structure to transition into its secondary defence line. At this point, the steel frame and the buckled bracing jointly bear the load, and the slope of the hysteresis curve outer contour slows but remains full. The hysteresis curve development trend of specimen BSD-2 is similar to that of specimen BSD-1. When loaded to 6 Δ_y, the model failed to converge because significant plastic deformation occurred at the middle horizontal position of the energy-dissipating steel strips. However, it can also be predicted that with the increasing loading displacement, specimen BSD-2 will exhibit bending buckling of the compressed bracing member and a reduction in bearing capacity.

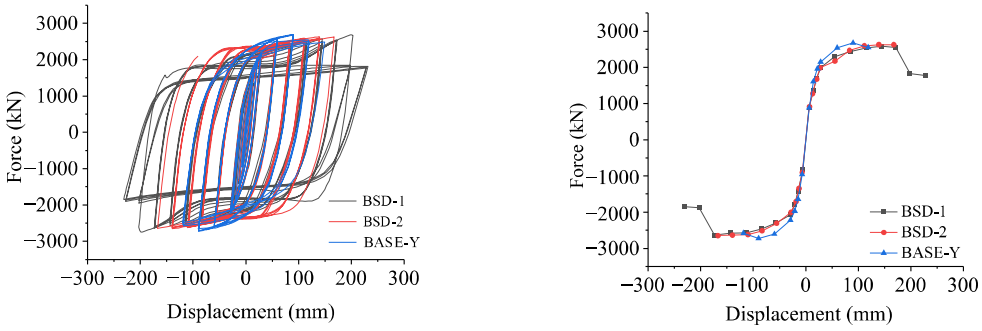

(**a**) Hysteresis curves (**b**) Backbone curves

Figure 12. Force-displacement curves of specimens BASE-Y, BSD-1, and BSD-2.

A comparison of the backbone curve in Figure 12b clearly reveals that the BASE-Y sample has the highest slope in the initial stages of loading, indicating a greater bearing capacity at low displacements. After the displacement reaches 3 Δ_y, the slope of the backbone curve begins to decrease until the sample fails. This decline is attributed to the web plate of the energy-dissipating beam section entering the plastic development phase

at low deformations due to shear action, leading to local buckling under the restraint of the flanges and stiffeners, which in turn results in a reduction in the bearing capacity. The initial trends of the backbone curves for BSD-1 and BSD-2 are roughly identical. However, upon reaching a loading displacement of 6 Δ_y, specimen BSD-1 experiences buckling of the compressed bracing member, leading to a significant reduction in the slope of the backbone curve.

The detailed mechanical performance indicators are presented in Table 6. The yield displacement (Δ_y), ultimate displacement (Δ_u), yield force (P_y), maximum force (P_{max}), and ductility capacity ($\mu = \Delta_u / \Delta_y$) are as follows: The yield forces of the three types of samples are essentially the same. However, the ductility coefficients of specimens BSD-1 and BSD-2 are increased by 59.57% and 39.47%, respectively, compared with those of sample BASE-Y, whereas their bearing capacities are reduced by 3.26% and 2.78%, respectively. This finding indicates that compared with the traditional YEBFs, the new type of YEBFs equipped with BSD dampers can significantly enhance the ductility of the structure at the expense of a minor reduction in the bearing capacity.

Table 6. Detailed parameters of BASE-Y, BSD-1, and BSD-2.

Specimen	Δ_y/mm	Δ_u/mm	P_y/kN	P_{max}/kN	μ
BASE-Y	28.32	118.45	2142.91	2724.74	4.18
BSD-1	29.77	187.80	2010.10	2635.80	6.67
BSD-2	28.65	167.11	1982.71	2648.83	5.83

4. Analysis of the Hysteresis Performance of the BSDF and TEBF

Previous research has shown that BSD-1 has superior ductility and sustained energy dissipation capabilities compared with BSD-2. Hence, in the modelling endeavours of this section, the specimen designated as BSD-1 was chosen as the representative damper for analysis. Two steel frames, each consisting of three story and one span, were constructed: one equipped with BSD-1 devices (BSDF) and the other a traditional eccentrically bare braced steel frame (TEBF). The dimensions of the beams and columns of the steel frames are consistent with those detailed in Section 3, with a story height of 3000 mm, and the steel material utilized is Q235. Before the experiments, monotonic loading was applied to both BSDF and TEBF to ascertain their yield displacements, which were determined to be 98 mm.

Both frames were subjected to fully fixed boundary conditions at the base of the columns, whereas lateral constraints in the X-direction were applied to both sides of the main beam. Coupling points were established in the Y-direction at the node domain on one side of the 3-story frame, where cyclic horizontal loads were applied. The loading method and grid division were consistent with those described in Section 3. Here, we chose only the grid division, and the boundary condition diagram of the BSDF is provided as an example, as shown in Figure 13.

4.1. Comparison of Stress Failure MODES

Figure 14 shows the stress cloud of the BSDF during cyclic loading. When the loading displacement reaches 1 Δ_y, the stress is predominantly concentrated in the steel strips of the BSD, whereas the stress levels in the frame beams, frame columns, and bracing are relatively low. When the load continues to 4 Δ_y, there is a significant increase in stress at the column bases, node domain, and flanges at the ends of the beams in the Y-axis direction, approaching the ultimate strength of the steel material. Notably, the stress increase is most pronounced near the column bases of the Y-axis frame beams on the 2nd story and 3rd story. This is attributed to the fact that during the loading process, the gusset plates are

welded to the frame columns and beams, leading to a substantial increase in the flexural stiffness of the frame beams at these locations, causing the plastic hinge that should have appeared at the node position to move towards the midspan of the beam. The stress on the flange of the beam rapidly increases. When loaded to 5 Δ_y, the stress values at the energy-dissipating steel strips are reduced. In contrast, the stress at the outer flanges at the lower ends of the first-story columns significantly increases. After the loading displacement reaches 6 Δ_y, the stress at the column bases further increases and extends continuously along the bracing members. Pronounced plastic hinges appear near the node domains of the Y-axis direction frame beams at each story, and the stress begins to develop from the flanges towards the webs.

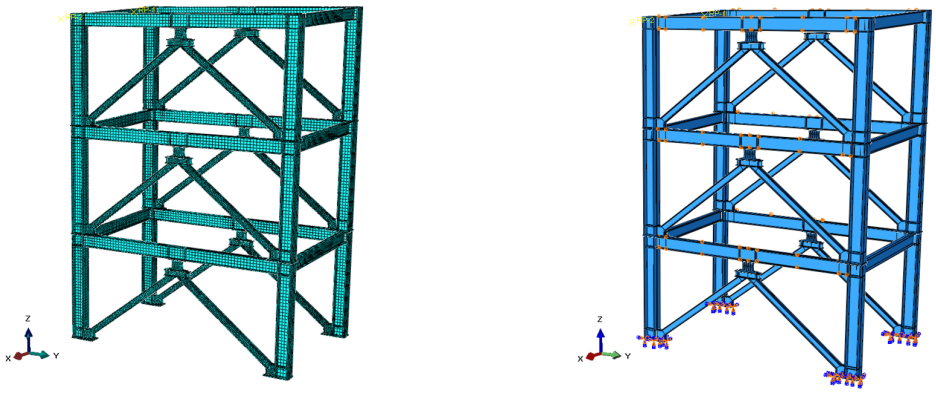

(**a**) Grid division (**b**) Boundary conditions

Figure 13. Grid division and boundary conditions of BSDF.

Figure 15 shows the stress cloud of the TEBF during cyclic loading. When the loading displacement reaches 1 Δ_y, the stress is primarily concentrated in the web region of the eccentrically braced energy-dissipating beam, and the stress near the gusset plates of the Y-axis frame beams also begins to gradually increase. When the load continues to 2 Δ_y, the stress in the web of the energy-dissipating beam approaches the ultimate strength of the steel, and the stress near the gusset plates of the Y-axis frame beams increases to the ultimate strength of the steel and develops towards the centre. When the displacement load reaches 3 Δ_y, the stress at the column bases and bracing feet increases significantly, and the web of the energy-dissipating beam sections on each story undergoes varying degrees of buckling, with the buckling degree being greatest on the 2nd story, followed by the 3rd story, and then the 1st story. When loaded to 4 Δ_y, the web of the energy-dissipating beam on each story experiences significant buckling deformation, and the compressed bracing members also experience out-of-plane instability. The stress at the bracing feet, both ends of the Y-axis frame beams, and the lower flanges at the midspan all reach the ultimate strength of the steel, causing the structure to lose its bearing capacity and fail.

In conclusion, a comparison of the stress clouds of the two steel frames mentioned above revealed that the stresses in the BSDF were primarily concentrated in the node domains, gusset plates, and near the gusset plates of the Y-axis frame beams, with a relatively uniform stress distribution throughout the loading process. In contrast, the TEBF steel framework experienced buckling of the energy-dissipating beam in the mid-to-late stages of loading, leading to structural instability and failure. Moreover, stresses at the energy-dissipating beam, bracing members and node domains significantly exceeded the ultimate strength of the steel material, thus failing to provide sustained energy dissipation capabilities.

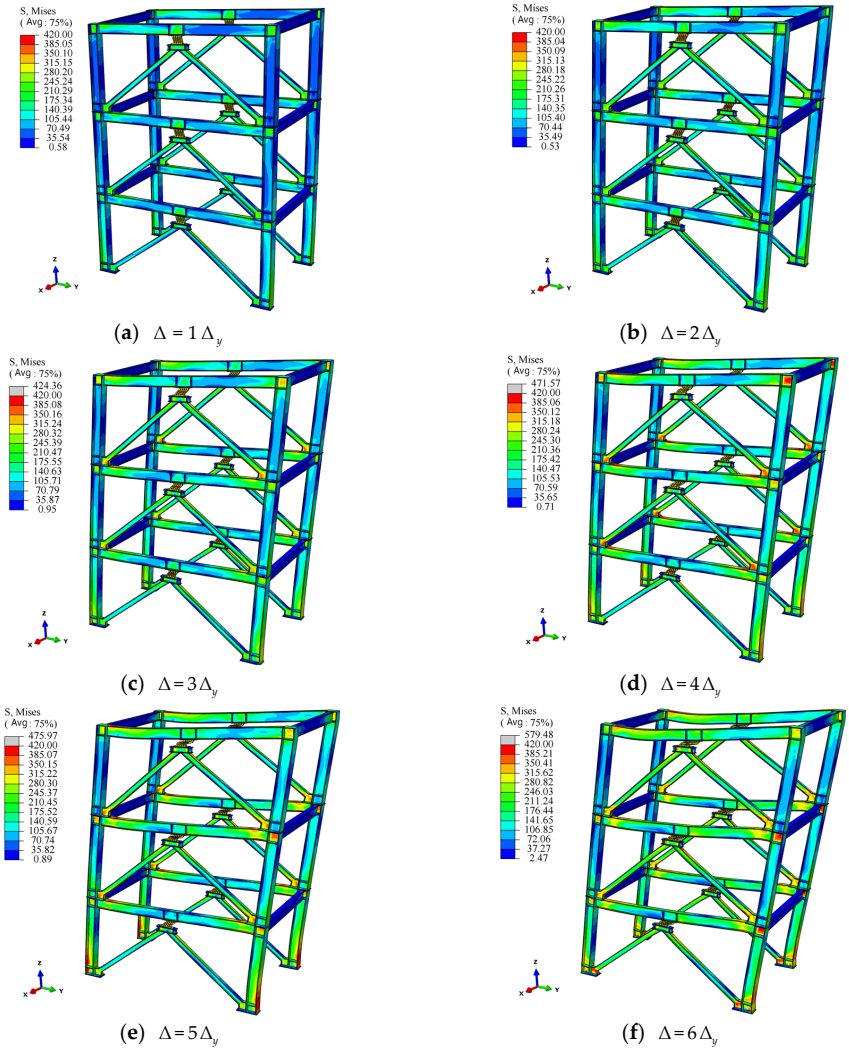

Figure 14. Stress cloud of BSDF during cyclic loading process.

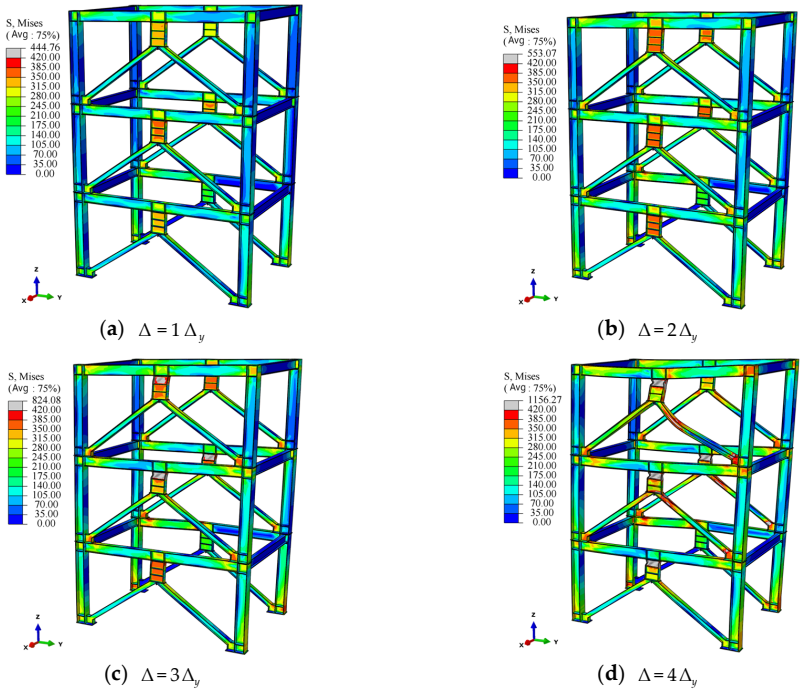

Figure 15. Stress cloud of TEBF during cyclic loading process.

4.2. Comparison of Force-Displacement Curves

Figure 16 shows the force-displacement curves for frames BSDF and TEBF. The hysteresis curve of TEBF approximates a shuttle shape, whereas the hysteresis curve of BSDF resembles a Z-shape. Figure 16a shows that during the initial loading stage, owing to the shear-type energy dissipation beam of the TEBF, it has a high bearing capacity under small deformations, resulting in a larger hysteresis loop envelope area than the frame BSDF. When the loading displacement reaches 150 mm, the hysteresis loop envelope area of the BSDF gradually increases, whereas the TEBF exits operation due to buckling of the energy dissipating beam, so its hysteresis curve envelope area slowly decreases. Figure 16b shows that before attaining the yield displacement, both the energy-dissipating beam and the BSD devices are in the elastic working stage, with their backbone curves essentially being consistent. When the loading displacement reaches 150 mm, the slope of the TEBF backbone curve becomes negative because the web plate of the energy-dissipating beam begins to enter the buckling stage, resulting in a rapid decrease in bearing capacity; conversely, the slope of the BSDF backbone curve consistently increases throughout the loading process, indicative of a stable bearing capability.

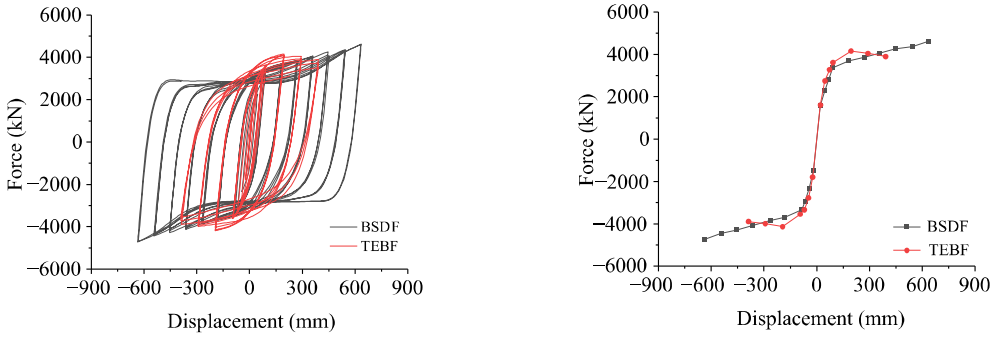

(**a**) Hysteresis curves (**b**) Backbone curves

Figure 16. Force-displacement curves for the BSDF and TEBF frames.

Table 7 shows the relevant indicators of bearing capacity and ductility. Under cyclic loading, the yield-bearing capacity and ultimate bearing capacity of BSDF increased by 3.13% and 11.12%, respectively, compared with those of TEBF, and the ductility coefficient increased by 56.7%. These findings indicate that the YEBFs with BSD devices have a relatively high bearing capacity and ductility.

Table 7. Parameters related to the bearing capacity and ductility.

Specimen	Δ_y/mm	Δ_u/mm	P_y/kN	P_{max}/kN	μ
BSDF	95.21	634.55	3414.07	4619.75	6.66
TEBF	92.00	391.36	3310.32	4157.13	4.25

4.3. Comparison of Stiffness Degradation and Strength Degradation

Figures 17 and 18 illustrate the stiffness degradation and strength degradation curves for BSDF and TEBF, respectively. Both frame types exhibit similar stiffness degradation trends; however, the BSDF frame has an initial stiffness of 7.68% greater than that of the TEBF frame, although the stiffness degradation rate for the BSDF frame is slightly greater than that of TEBF. When the loading displacement is less than 150 mm, the strength of the BSDF frame tends to increase. In contrast, strength degradation begins for the BSDF frame when the loading displacement exceeds 150 mm, whereas the TEBF frame starts to experience strength degradation at a loading displacement of 100 mm.

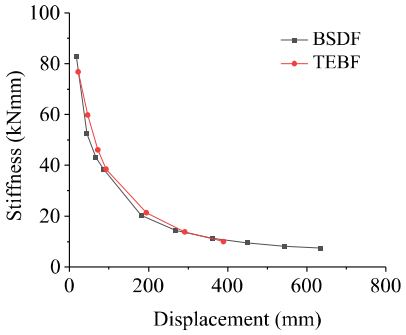

Figure 17. Stiffness degradation curves.

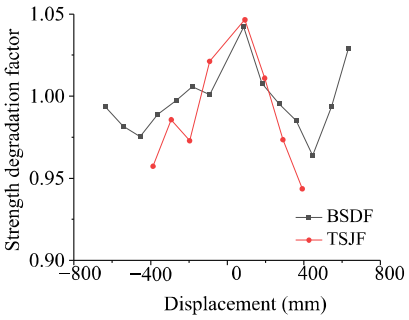

Figure 18. Strength degradation curves.

4.4. Comparison of Energy Dissipation Capacity

Figure 19 provides a comparison of the energy dissipation capacities of the BSDF and TEBF. The comparison is specifically conducted by evaluating the equivalent viscous damping coefficients and energy dissipation at various loading displacements. As illustrated in Figure 19a, under cyclic loading, the equivalent viscous damping coefficients for both frame types initially increase and then decrease, with the inflection point occurring at a displacement of approximately 300 mm. Figure 19b clearly shows that the TEBF results in higher energy dissipation values than the BSDF frame does when the loading displacement is less than 4 Δ_y. However, with further increases in loading displacement, buckling initiates in the web of the energy dissipation beam section of the TEBF, whereas the BSDF demonstrates a sustained capacity for energy dissipation.

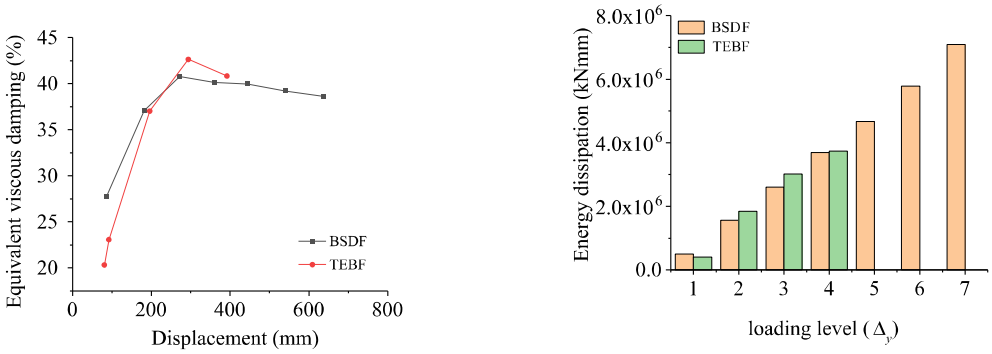

(**a**) Equivalent viscous damping coefficient (**b**) Energy dissipation

Figure 19. Comparison of energy dissipation capacity.

As mentioned above, the BSDF has a higher bearing capacity and ductility, as well as a higher energy dissipation capacity than the TEBF.

5. Conclusions

This paper investigated the effect of BSDs on the hysteresis performance of multi-story YEBFs. The existing model was validated through FE analysis. A BSD-YEBFs model was subsequently established, and the seismic performance parameters of multi-story YEBFs under cyclic loading were analysed, with a focus on the impact of BSD devices. The main conclusions obtained are as follows:

1. FE verification was conducted on the samples in the existing single-span, two-story frame test, and the FE simulation and experimental results were roughly the same, with relevant mechanical performance parameter errors within a reasonable range. A correct modelling approach for the YEBFs was provided.
2. Compared with those of BASE-Y, the ductility coefficients of BSD-1 and BSD-2 were increased by 59.57% and 39.47%, respectively, whereas the corresponding bearing capacities were reduced by 3.26% (P_y) and 2.78% (P_{max}), respectively. This finding indicates that the equipment of BSD devices in YEBFs can significantly enhance structural ductility with only a minor sacrifice in bearing capacity.
3. During the cyclic loading process, although the energy dissipation of the TEBF is slightly greater than that of the BSDF in the early and middle stages (displacements less than 4 Δ_y), as loading continues (approximately 4 Δ_y), the web of the energy dissipating beam in the TEBF buckles successively, leading to structural instability and failure. In contrast, the stress distribution in the BSDF remains more uniform throughout the loading process. Furthermore, compared with TEBF, BSDF increased its yield bearing capacity by 3.13%, ultimate bearing capacity by 11.12%, and ductility coefficient by 56.7%. The initial stiffness of the BSDF was also 7.68% higher than that of the TEBF. In summary, YEBFs with BSD devices exhibit superior bearing capacity, ductility, and more sustained energy dissipation capabilities than traditional YEBFs do.

Author Contributions: Conceptualization, C.Z.; methodology, H.Z. (Hong Zheng); software, X.X.; validation, J.Z. and L.J.; formal analysis, C.Z.; investigation, C.Z.; resources, L.J.; data curation, H.W.; writing—original draft preparation, X.X. and H.W.; writing—review and editing, C.Z. and H.W.; visualization, Y.T.; supervision, M.L.; project administration, X.W. and H.Z. (Hai Zhang); funding acquisition, C.Z. All authors have read and agreed to the published version of the manuscript.

Funding: This research received no external funding.

Data Availability Statement: The raw data supporting the conclusions of this article will be made available by the authors on request.

Acknowledgments: Special thanks to H.Z. (Hong Zheng) for theoretical support and X.X. for writing the original draft of this article.

Conflicts of Interest: Authors Jing Zhao and Xiyao Wang were employed by the 3rd Construction Co., Ltd., China Construction 5th Engineering Bureau. Authors Yuxiao Tian, Muhua Liang and Hai Zhang were employed by the China Railway Urban Construction Group Co., Ltd. The remaining authors declare that the research was conducted in the absence of any commercial or financial relationships that could be construed as a potential conflict of interest.

References

1. Chen, X.; Li, S.; Liang, G.; He, M. Numerical Parameter Analysis of High-Strength Steel Frame with Y-Eccentric Brace Using Variable Replaceable Link. *Buildings* **2024**, *14*, 2149. [CrossRef]
2. Wasse, A.D.; Dai, K.; Wang, J.; Sharbati, R. State-of-the-art review: Seismic design and performance assessment of special concentrically braced frames developed for complex industrial building structures. *Int. J. Steel Struct.* **2024**, *24*, 280–295. [CrossRef]
3. Hjelmstad, K.D.; Popov, E.P. Characteristics of eccentrically braced frames. *J. Struct. Eng.* **1984**, *110*, 340–353. [CrossRef]

4. Zhuang, L.; Wang, J.; Nie, X.; Wu, Z. Experimental study on seismic behaviour of eccentrically braced composite frame with vertical LYP steel shear link. *Eng. Struct.* **2022**, *255*, 113957. [CrossRef]
5. Abdelhamid, F.; Yahiaoui, D.; Saadi, M.; Lahbari, N. Lateral reliability assessment of eccentrically braced frames including horizontal and vertical links under seismic loading. *Eng. Technol. Appl. Sci.* **2022**, *12*, 8278–8283. [CrossRef]
6. Xiao, X.; Zhang, P.; Zhang, Q. Seismic Energy Dissipation Analysis of Y And K Type Composite Eccentrically Braced Steel Frames. *IOP Conf. Ser. Earth Environ. Sci.* **2018**, *153*, 032015. [CrossRef]
7. Li, T.; Su, M.; Guo, J.; Zhao, K.; Zhang, Q. Seismic performance evaluation of Y-shaped eccentric brace–high-strength steel frame structure based on remote collaborative hybrid test. *Soil. Dyn. Earthq. Eng.* **2023**, *164*, 107621. [CrossRef]
8. Xu, J.; Wang, S.L.; Mohamed, H.S.; Han, J.; Han, Z.; Tu, J.; Li, Z. Seismic performance of shear energy dissipation beams in D-shaped eccentrically braced steel frames. *J. Constr. Steel Res.* **2021**, *180*, 106584. [CrossRef]
9. Liu, B.; Lu, Y.; Li, W.; Li, J.; Zhao, J.; Wang, S.; Ni, G.; Meng, Q. Study on Seismic Behavior of Different Forms of Eccentrically Braced Steel Frames. *Buildings* **2024**, *14*, 2064. [CrossRef]
10. Zheng, W.; Shen, L. Seismic performance of high strength steel frames with different eccentric braces based on PBSD method. *World Earthq. Eng.* **2020**, *36*, 80–92. (In Chinese)
11. Wang, F.; Su, M.; Hong, M.; Guo, Y.; Li, S. Cyclic behaviour of Y-shaped eccentrically braced frames fabricated with high-strength steel composite. *J. Constr. Steel Res.* **2016**, *120*, 176–187. [CrossRef]
12. Ashrafi, A.; Imanpour, A. Seismic response of steel multi-tiered eccentrically braced frames. *J. Constr. Steel Res.* **2021**, *181*, 106600. [CrossRef]
13. Pourzangbar, A.; Vaezi, M.; Mousavi, S.M.; Saber, A. Effects of brace-viscous damper system on the dynamic response of steel frames. *Int. J. Eng.* **2020**, *33*, 720–731.
14. Piluso, V.; Montuori, R.; Nastri, E.; Paciello, A. Seismic response of MRF-CBF dual systems equipped with low damage friction connections. *J. Constr. Steel Res.* **2019**, *154*, 263–277. [CrossRef]
15. Khazaei, M. Investigation on dynamics nonlinear analysis of steel frames with steel dampers. *Procedia Eng.* **2013**, *54*, 401–412. [CrossRef]
16. Zhao, J.; Tao, M.; Zhuang, L. Development of bent shear panel dampers for eccentrically braced composite frames. *J. Constr. Steel Res.* **2022**, *193*, 107292. [CrossRef]
17. Li, Y.; Wang, W.; Su, S.; Quan, C.; Xu, J.; Jia, Y.; Mi, J. Seismic performance assessment of eccentrically braced steel frame using demountable-metallic-corrugated-shear-panel dampers. *J. Constr. Steel Res.* **2023**, *207*, 107972. [CrossRef]
18. Mirzai, N.M.; Attarnejad, R.; Hu, J.W. Enhancing the seismic performance of EBFs with vertical shear link using a new self-centering damper. *Int. J. Earthq. Eng.* **2018**, *35*, 57–75.
19. Soltani, S.; Javaheri-Tafti, M.R.; Vetr, M.Q. Experimental and analytic study of seismic resistant eccentrically braced frames with dissipative devices. *J. Build. Pathol. Rehabil.* **2025**, *10*, 28. [CrossRef]
20. Ashtari, M.; Lari, S.; Çağlar, H.; Pouraminian, M.; Salmani, R.; Genjaly, A. Development and performance evaluation of an auxetic yield metal damper for enhanced seismic energy dissipation. *Structures* **2025**, *71*, 107892. [CrossRef]
21. Amiri, H.A.; Najafabadi, E.P.; Estekanchi, H.E. Experimental and analytical study of Block Slit Damper. *J. Constr. Steel Res.* **2018**, *141*, 167–178. [CrossRef]
22. Javanmardi, A.; Ibrahim, Z.; Ghaedi, K.; Benisi Ghadim, H.; Hanif, M.U. State-of-the-art review of metallic dampers: Testing, development and implementation. *Arch. Comput. Methods Eng.* **2020**, *27*, 455–478. [CrossRef]
23. Amiri, H.A.; Najafabadi, E.P.; Estekanchi, H.E.; Ozbakkaloglu, T. Performance-based seismic design and assessment of low-rise steel special moment resisting frames with block slit dampers using endurance time method. *Eng. Struct.* **2020**, *224*, 110955. [CrossRef]
24. Mohseni, P.K.; Zahedi-khameneh, A.; Naeemifar, O. Study of the effect of geometric parameters of steel block slit dampers on energy absorption. *Int. J. Steel Struct.* **2020**, *20*, 1069–1079. [CrossRef]
25. Shen, M. Behavior Study of Y-Eccentrically Braced Steel Frames Under Cyclic Load Considering Length Changed of Link Beam. Master's Thesis, Suzhou University of Science and Technology, Suzhou, China, 2008. (In Chinese)
26. *GB 50011-2010*; Code for Seismic Design of Buildings. China Architecture and Building Press: Beijing, China, 2016.
27. *JGJ 99-2015*; Technical Specification for Steel Structure of Tall Building. China Building Industry Press: Beijing, China, 2015.
28. *GB 50017-2017*; Steel Structure Design Standard. China Planning Press: Beijing, China, 2017.
29. Su, M.; Gu, Q.; Shen, L. Finite element analysis of steel members under cyclic loading. *J. Eng. Mech.* **2001**, *18*, 51–59. (In Chinese)

30. *JGJ 101-96*; Specification of Testing Methods for Earthquake Resistant Building. China Academy of Building Research: Beijing, China, 1997.
31. Meng, L. The Analysis and Design Criteria of Y Style Eccentrically Braced Steel Frames under Cyclic Load. Master's Thesis, Xi'an University of Architecture and Technology, Xi'an, China, 2005. (In Chinese)